

# A seven-facet polyhedron captures the composition-only formation-energy landscape of inorganic solids

Justin Tahmassebpur,<sup>1</sup> Sarvesh Chaudhari,<sup>2</sup> Cristobal Mendez,<sup>1</sup> Rushil Choudhary,<sup>2</sup> Sudipta Kundu,<sup>3</sup> Raymond E. Schaak,<sup>3</sup> Héctor Abruña,<sup>4</sup> Peter Frazier,<sup>5</sup> and Tomás Arias<sup>2</sup>

<sup>1</sup>*Department of Applied and Engineering Physics, Cornell University*

<sup>2</sup>*Department of Physics, Cornell University*

<sup>3</sup>*Department of Chemistry, Pennsylvania State University*

<sup>4</sup>*Department of Chemistry and Chemical Biology, Cornell University*

<sup>5</sup>*School of Operations Research and Information Engineering, Cornell University*

(Dated: February 3, 2026)

This work demonstrates that the convex hull of formation energies for solid compounds involving elements from hydrogen to uranium admits a remarkably simple description over the 92-dimensional space of chemical compositions, despite the enormous combinatorial complexity of possible atomic structures. By training an interpretable max-affine model directly on near-hull formation energies from the Materials Project density-functional theory (DFT) database, we find that the hull can be reconstructed to DFT accuracy using a polyhedron with only seven facets. These facets define seven chemically coherent materials classes, with just seven coefficients per element sufficing to capture the dominant energetic trends across composition space. Remarkably, this compact, composition-only representation generalizes far beyond bulk formation energies. Without retraining or structural input, the same model reproduces trends in DFT-calculated defect formation energies, captures experimentally observed elemental mixing correlations in high-entropy materials, and enables the construction and optimization of Pourbaix diagrams for electrochemical stability. Together, these results show that many materials properties governed by energy differences can be expressed as simple linear combinations of a small set of interpretable, element-specific parameters. The result is a bonding-geometry-free thermodynamic framework that unifies stability, defects, mixing, and electrochemistry, and enables rapid, interpretable screening across vast chemical spaces.

A central challenge in materials physics is to understand what determines the thermodynamic stability of solid compounds across the vast space of possible chemical compositions [1, 2]. Stability is governed by the convex hull of formation energies, which defines the lowest-energy realizable materials and separates stable compounds from those unstable with respect to phase separation [2, 3]. Formally, the convex hull may be viewed as a function of composition,  $\text{Hull}[E(\mathbf{x})]$ , where  $\mathbf{x}$  denotes the stoichiometry of a material. Here,  $\mathbf{x}$  is a 92-dimensional vector of elemental fractions,  $\text{H}_{x_1}\text{He}_{x_2} \dots \text{U}_{x_{92}}$ , and the formation energy is defined as

$$E(\mathbf{x}) \equiv \min_n E(S_n(\mathbf{x})), \quad (1)$$

the minimum over all locally stable atomic arrangements  $S_n(\mathbf{x})$  at fixed composition.

In principle, identifying this minimum requires exploring a combinatorially large set of metastable structures for each composition [4, 5]. Although large-scale density functional theory (DFT) searches can address individual compositions, the exponential growth of candidate structures renders exhaustive enumeration across chemical space intractable [4, 6]. This combinatorial barrier has long defined the practical limits of materials discovery.

Machine learning has substantially accelerated this process by learning surrogate models from large databases of DFT-calculated energies [2, 3, 7–10].

Geometry-aware models, including graph neural networks (GNNs), now achieve near-DFT accuracy for formation energies and related properties across diverse materials classes [11–16]. However, these approaches still require explicit structural input and therefore inherit the underlying search over  $\{S_n(\mathbf{x})\}$ . Generative models, such as diffusion-based crystal generators [17], further accelerate discovery by proposing plausible candidate structures; however, at a fixed composition, the energies of many such candidates must still be evaluated to identify the most stable phase. Thus, while machine learning reduces computational cost, it does not eliminate the combinatorial complexity of atomic structure space.

Against this backdrop, an unexpected result has emerged: material formation energies can often be predicted accurately from composition alone, without any explicit structural information. Beginning with EllemNet [18] and followed by Roost [19], IRNet [20], and CrabNet [21], deep neural networks have demonstrated that composition-only inputs suffice to reproduce DFT-calculated formation energies across vast chemical spaces. These models are trained to approximate the full composition–energy function  $E(\mathbf{x})$ , from which the convex hull may be derived. Their success is striking: they achieve high accuracy despite never exploring the exponentially large set of atomic configurations  $\{S_n(\mathbf{x})\}$  that formally defines  $E(\mathbf{x})$ .

This empirical success suggests a deeper and more fundamental possibility: that the mapping from composi-

tion to formation energy—particularly the convex hull  $\text{Hull}[E(\mathbf{x})]$ —may possess an intrinsic simplicity that is not apparent from its combinatorial definition. This raises a foundational question: *is the convex hull of formation energies governed by a simple, interpretable function of composition?*

Here, we show that the answer is *yes*. We first demonstrate that near-hull formation energies can be predicted with near-DFT accuracy using a compact, three-hidden-layer perceptron trained solely on composition. Despite its shallow architecture and dramatically reduced parameter count compared with existing composition-only models, this network accurately reproduces Materials Project formation energies in the vicinity of the convex hull, indicating that the relevant composition–energy landscape is far simpler than its structural origins suggest.

Building on this observation, we further show—remarkably—that the Materials Project formation-energy convex hull, spanning more than 50,000 bulk compounds, can be reproduced by a polyhedron with only *seven* facets. To identify this structure, we introduce an extremely compact and interpretable max-affine model in which each element in the periodic table is described by only seven learned coefficients. Despite its minimal parameterization, with 645 linear coefficients accurately describing over 50,000 materials, this model captures systematic energetic trends across diverse chemistries, reframing composition-only prediction as a low-dimensional geometric description of collective materials stability.

Finally, we demonstrate that both the compact neural network and the max-affine model generalize beyond formation energies to reproduce key physical trends across multiple domains, including DFT-calculated point defect energetics, experimental spatial correlations in high-entropy phosphide nanoparticles, and electrochemical stability encoded by Pourbaix diagrams. Together, these results reveal an unexpected geometric simplicity underlying materials thermodynamic stability and enable rapid, interpretable materials screening in regimes governed by energy-based descriptors—for example, in the design of oxygen diffusion barrier materials, where defect formation energies play a central role [22].

## RESULTS

### Models and Formation Energies

To explore the simplicity of the Materials Project formation energy convex hull, we first trained a shallow three-layer neural network with 512 units per layer and tanh activations to learn the formation energies of materials within 0.25 eV/atom of the convex hull. The threshold of 0.25 eV/atom was chosen because it yielded the

best performance for the applications considered in this work. To ensure a one-to-one mapping between composition and energy, we consider only the lowest-energy structure in the database for each composition so as to best represent  $E(\mathbf{x}) \equiv \min_n E(S_n(\mathbf{x}))$ . The final training set consists of 86,925 materials.

The direct input to our network is simply  $\mathbf{x}$ , the 92-dimensional vector whose entries correspond to the atomic fractions of each element in the material,  $\text{H}_{x_1}\text{He}_{x_2}\dots\text{U}_{x_{92}}$ . For example, the compound  $\text{Li}_{0.33}\text{Be}_{0.33}\text{B}_{0.33}$  is represented as  $x_3 = 0.333\dots$ ,  $x_4 = 0.333\dots$ , and  $x_5 = 0.333\dots$ , with all other components of  $\mathbf{x}$  equal to zero. Fig. 1a shows the performance of the network and that, despite being shallow, it achieves an MAE of 0.044 eV/atom, within DFT accuracy.

The ability of a shallow network to recover formation energies near the convex hull suggests that the underlying landscape may be simpler than expected. Motivated by this observation, we further explore this simplicity using the following max-affine model to approximate the formation energy of materials on the Materials Project [2] convex hull:

$$E(\mathbf{x}) = \max_{f=1}^F \left( \sum_{s=1}^{92} a_{f,s} x_s \right) + b, \quad (2)$$

where  $\mathbf{x}$  is the 92-dimensional composition vector, and  $a_{f,s}$  and  $b$  are learned coefficients. The max-affine model is convex by construction, and with a sufficiently large number of facets  $F$ , it can in principle recover the true Materials Project convex hull. We train this model on all lowest-energy structures within 0.025 eV/atom of the convex hull. This value is approximately the thermal energy at room temperature, and well within DFT accuracy. This ensures the model is trained on compositions sufficiently close to the hull to accurately capture its underlying shape. This threshold roughly doubles the number of materials in the training set compared to using only those exactly on the hull, increasing the amount of training data available while preserving proximity to the hull and improving the statistical coverage of the approximation.

The resulting dataset comprises 51,068 bulk formation energies for compounds on or near the Materials Project [2] convex hull. Figure 1b shows the performance of the max-affine model, Eq. (2), as a function of the number of facets  $F$  for models trained with  $F = 1, \dots, 64$ . Increasing  $F$  systematically reduces the test error, reflecting the added expressive power of additional facets. We select  $F = 7$  as an optimal balance between simplicity and accuracy, where the test error has largely saturated and additional facets yield diminishing returns while substantially reducing interpretability. The corresponding test-set performance for the seven-facet model is shown in Fig. 1c, yielding a mean absolute error of 0.076 eV/atom, within typical DFT accuracy. Although reproducing the

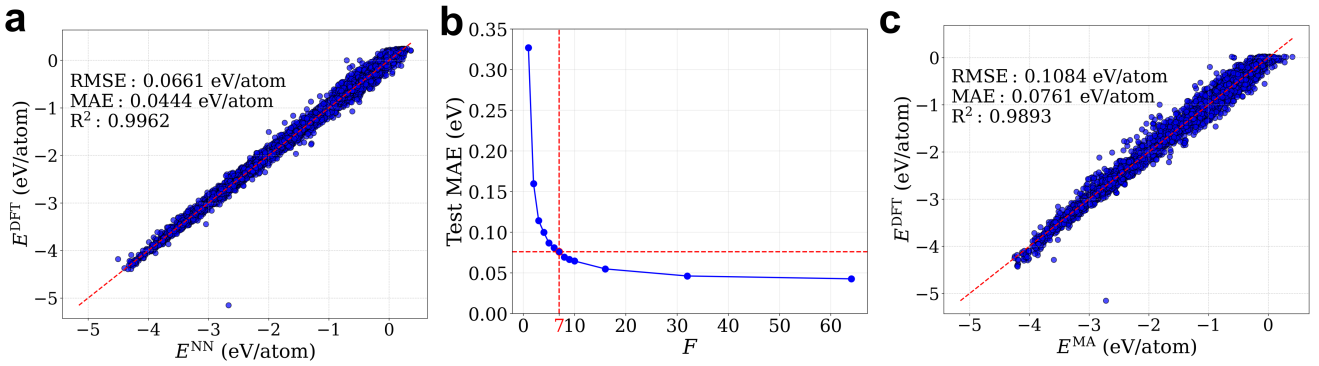


FIG. 1. Performance of composition-only models on formation-energy prediction. **a** Test-set neural network predictions versus DFT-computed formation energies from the Materials Project [2]. The red line indicates perfect agreement ( $y = x$ ). **b** Test-set mean absolute error (MAE) of the max-affine model as a function of the number of facets  $F$ , with the chosen value  $F = 7$  indicated by the red lines. **c** Test-set max-affine model predictions versus DFT-computed formation energies from the Materials Project [2]. The red line indicates perfect agreement ( $y = x$ ).

exact Materials Project convex hull would require more facets, accurate prediction of formation energies—and, as shown below, of trends in defect energetics and other energy differences—does not.

### Interpretability

Our max-affine model assigns each material in the Materials Project to one of the seven facets. For any material with stoichiometry  $\mathbf{x}$ , the active facet is

$$f^* = \arg \max_f \sum_{s=1}^{92} a_{f,s} x_s.$$

Once this facet is identified, the corresponding linear coefficients determine, within that facet, the effective compositional chemical potentials for adding or removing atoms of each species:

$$\tilde{\mu}_s = \frac{\partial E(\mathbf{x})}{\partial x_s} = a_{f^*,s},$$

where  $E$  is the energy per atom of the material. Below, we refer to these quantities as *compositional chemical potentials* or, simply, *chemical potentials*. A key consequence of this interpretation of the model coefficients is that all materials lying on the same facet inherit the *same* facet-specific compositional chemical potentials. Thus, every facet represents a distinct and coherent bonding chemistry, and the max-affine model organizes the Materials Project into seven major classes of materials with closely related chemical behavior.

Figure 2 provides a chemical interpretation of the seven facets by visualizing how each facet organizes all stable (or nearly stable, within 0.025 eV/atom) binary materials in the Materials Project. To classify the materials, we first partition the elements into four main categories  $C$  according to their valence electronic structure

$C \in \{s, d/f, \text{early } p \text{ block, late } p \text{ block}\}$ . Then, for each facet  $f$  we consider the participation of each element  $E$  in compounds on that facet, and how often it bonds with elements from each of the four valence categories.

To make these facet-specific bonding patterns quantitative, we construct a normalized measure of how frequently each element participates in binaries with elements from different valence categories on each facet. Specifically, for each element  $E$  we compute  $w_{E,C}^f$ , defined as the sum of the atomic fractions of  $E$  in all binaries on facet  $f$  where the other element belongs to category  $C$ . This quantity represents the stoichiometric weight of element  $E$  on facet  $f$  in compounds formed with category  $C$ . To compare the relative representation of  $E$ - $C$  compounds across facets, we normalize by the total  $E$ - $C$  stoichiometric weight over all facets, defining  $\tilde{w}_{E,C}^f = w_{E,C}^f / \sum_{f'} w_{E,C}^{f'}$ . Because some facets are less represented in the Materials Project than others, we further normalize these values on each facet by their maximum,  $I_{E,C}^f = \tilde{w}_{E,C}^f / \max_{E',C'} \tilde{w}_{E',C'}^f$ . The resulting quantities indicate, within each facet, how strongly each element is represented in compounds formed with elements from each of the four categories.

Figs. 2a–g present facet-resolved maps for facets 1–7, each rendered as a periodic table. In these visualizations, the border color of each element indicates its valence category (blue:  $s$  block; green:  $d/f$  block; orange: early  $p$  block; red: late  $p$  block). Within each element cell, the interior is subdivided into four squares—one for each category—colored using the same scheme as the borders. For a given facet  $f$ , the intensity of the square corresponding to category  $C$  for element  $E$  is given by  $I_{E,C}^f$ , indicating how frequently element  $E$  forms binary compounds with elements from category  $C$  on that facet.

Figure 2 reveals that each facet exhibits a distinct and chemically coherent signature, which can be broadly

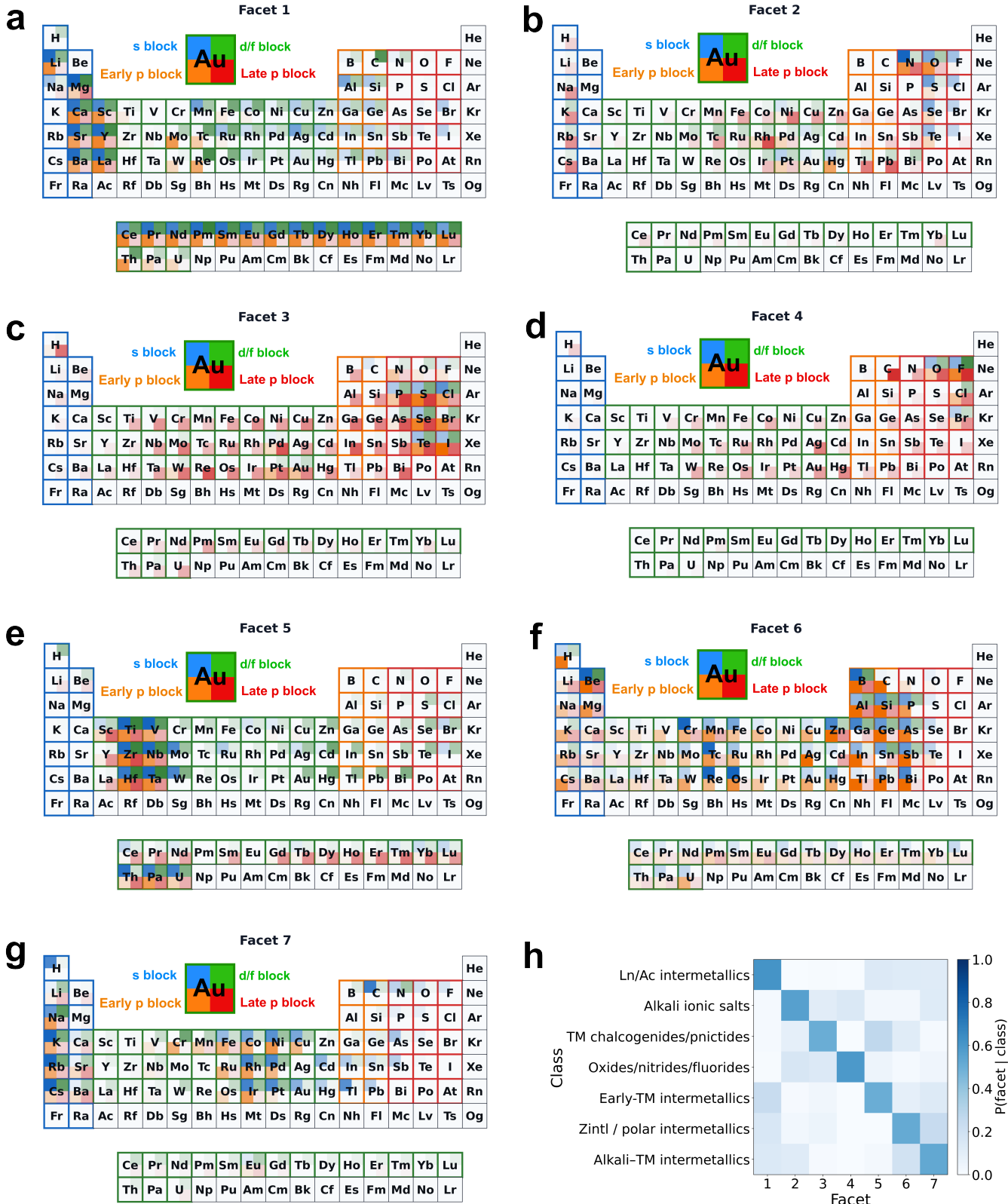


**FIG. 2. Chemical interpretation of max-affine facets for binary compounds.** **a–g** Facet-resolved periodic-table maps for facets 1–7 of the max-affine hull. As indicated by the enlarged element key, the border color of each element denotes its valence category (blue: *s* block; green: *d/f* block; orange: early *p* block; red: late *p* block). Within each element box, the four colored quadrants indicate how frequently that element forms binary compounds with elements from each category on the corresponding facet. **h** Facet–materials-class correlation matrix, where color intensity denotes the probability that a binary compound from a given materials class activates each facet.

summarized by the following dominant material classes. Facet 1 is enriched in lanthanide and actinide intermetallics with strongly metallic  $d/f-d/f$  or  $d/f-s$  bonding. Facet 2 highlights classic alkali ionic salts, such as Li–O/N/S/Se/F/Cl/Br compounds. Facet 3 captures transition-metal chalcogenides and pnictides, while Facet 4 corresponds primarily to mixed ionic–covalent oxides, nitrides, and fluorides involving  $p$ -block and transition-metal cations. Facet 5 is dominated by early transition-metal intermetallics. Facet 6 is enriched in binaries between alkali or alkaline-earth metals and early  $p$ -block elements, including many Zintl-like and polar  $s-p$  intermetallic semiconductors. Facet 7 reflects metallic alkali–transition-metal and alkali–alkali binaries. Together, these signatures demonstrate that the facet vectors do not partition composition space arbitrarily, but instead align with well-established chemistries.

To summarize and quantify the chemical structure apparent in the facet-resolved maps, we assign each binary compound to one of seven broad materials classes informed by the dominant patterns observed in Fig. 2a–g and evaluate  $P(f \mid \text{class})$ , the probability that a member of a given class activates facet  $f$ . The resulting correlation matrix (Fig. 2h) exhibits a pronounced diagonal structure, reflecting the fact that each class is dominated by a single facet. This analysis provides a compact chemical summary of the material classes uncovered by the max-affine model and reinforces that the learned facets align with recognizable chemical behavior.

This facet structure has direct physical meaning. Because the facet coefficients  $a_{f,s}$  define the effective chemical potentials  $\tilde{\mu}_s$  for all materials on facet  $f$ , members of a given facet share a common chemical fingerprint. Consequently, materials grouped together by the model are expected to exhibit similar trends in any property governed by energy differences. This insight provides the foundation for our subsequent results. Remarkably, the same max-affine model—trained solely on bulk formation energies—can be used *without retraining* to capture systematic trends in defect formation energies, spatial correlations in high entropy materials, and electrochemical stability. In the following section, we show how the facet-dependent chemical potentials furnish a compact, interpretable framework for predicting substitution, vacancy, and interstitial energetics across chemically diverse materials.

### Defect Energies

The max-affine and neural network models can be used for much more than formation-energy prediction alone, provided one is sufficiently creative in forming energy differences. Here, we demonstrate that the max-affine and neural network models reproduce trends in DFT-calculated defect energies, despite being trained only on

bulk formation energies. We consider three defect types that probe distinct compositional perturbations of a host lattice: substitutional, vacancy, and interstitial defects.

To predict the energies of such defects, we define compositional chemical potentials using a notation in which the chemical species appears as a subscript and the thermodynamic context appears as a superscript,  $\tilde{\mu}_{[\text{species}]}^{[\text{context}]}$ . We define the chemical potential of element A in the context of a material M as

$$\tilde{\mu}_A^M \equiv \frac{\partial}{\partial x_A} \left( \max_f \left[ \sum_s a_{f,s} x_s(M) + b \right] \right) = a_{f_M, A}, \quad (3)$$

where  $\mathbf{x}(M)$  denotes the composition of material M and  $f_M$  is the active facet for that composition. Here, M may represent a multicomponent material, for example  $A_x B_{1-x}$ . In the special case where the material consists of a single element,  $M = A$ , we omit the superscript and write the compositional chemical potential simply as  $\tilde{\mu}_A$ .

We now show that the energies of all three prototypical point defects—substitutional, vacancy, and interstitial—can be expressed entirely in terms of the effective compositional chemical potentials, beginning with substitutional defects. The substitution energy quantifies the cost of replacing one A-type atom in a host by a B-type atom. In a standard *ab initio* calculation, this is approximated using an  $n$ -atom periodic supercell and computed as

$$E_{\text{sub}}^n(A \leftarrow B) = E(A_{n-1}B) + E(A) - (E(A_n) + E(B)), \quad (4)$$

where  $E(M)$  represents the energy of one formula unit of M as written. The max-affine model can effectively realize the  $n \rightarrow \infty$  limit—the true dilute defect in an infinite host—for which the substitution energy is the compositional derivative of the formation energy,

$$E_{\text{sub}}^{\infty}(A \leftarrow B) = E(A) - E(B) + \partial_x^+ E(A_{1-x}B_x)|_{x=0}, \quad (5)$$

where  $\partial_x^+$  is a forward derivative with respect to  $x$  (see Methods for derivation). Substituting the max-affine model Eq. (3) gives

$$E_{\text{sub}}^{\text{MA}}(A \leftarrow B) = \tilde{\mu}_B^A - \tilde{\mu}_B. \quad (6)$$

Interstitial energies measure the cost of inserting a foreign atom into an otherwise pristine lattice. In practice, this is calculated as

$$E_{\text{int}}^n(A \leftarrow B) = E(A_nB) - (E(A_n) + E(B)), \quad (7)$$

and becomes in the dilute limit (see Methods),

$$E_{\text{int}}^{\infty}(A \leftarrow B) = E(A) - E(B) + \partial_x^+ E(A_{1-x}B_x)|_{x=0}, \quad (8)$$

which has the same mathematical form as the dilute-limit substitution energy, Eq. (5). Substituting the max-affine model yields

$$E_{\text{int}}^{\text{MA}}(A \leftarrow B) = \tilde{\mu}_B^A - \tilde{\mu}_B. \quad (9)$$

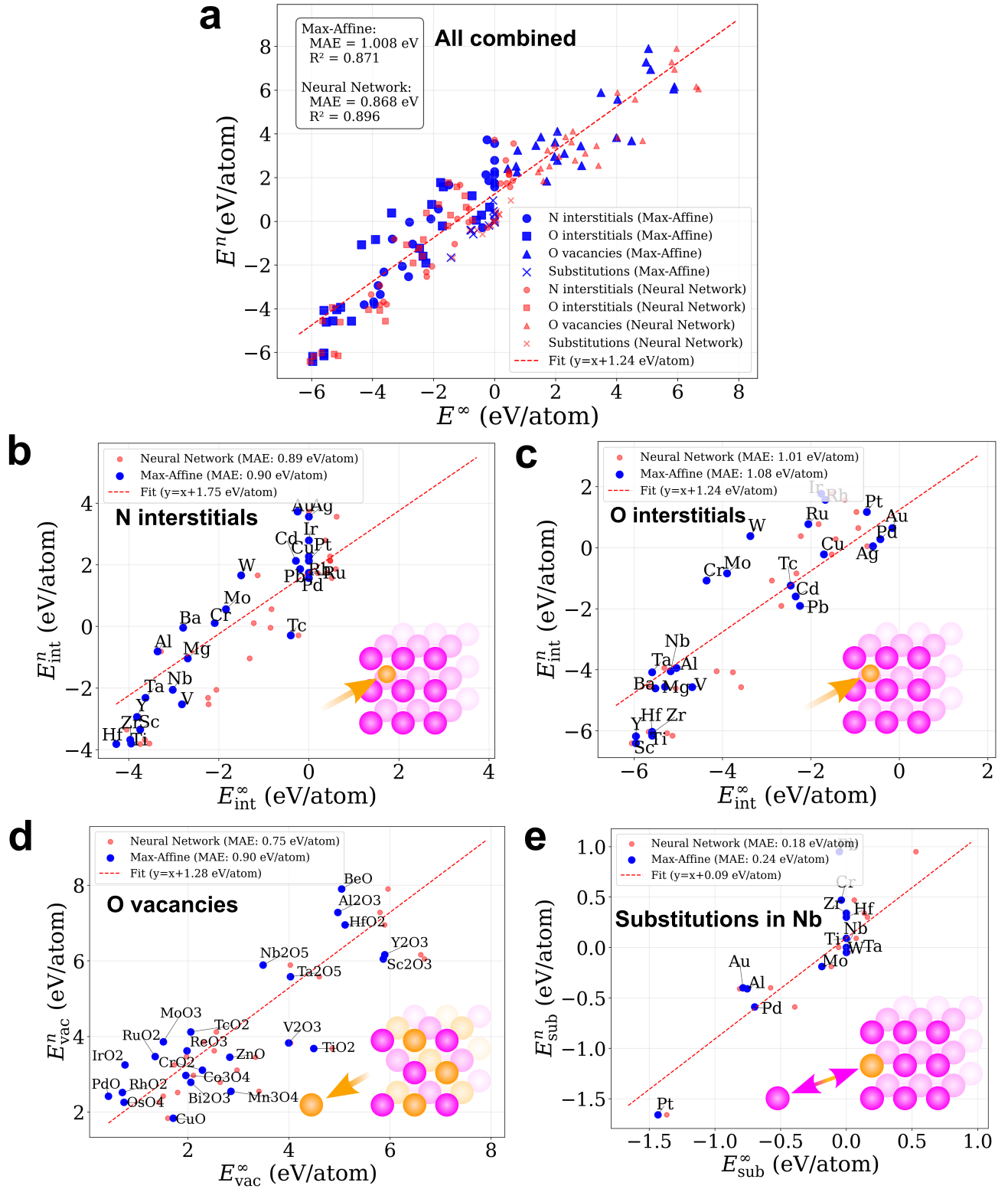


FIG. 3. **DFT-calculated versus predicted defect energies.** Perfect agreement, up to a constant offset, is indicated by the red dashed reference lines ( $y = x + C$ ). These are true out-of-distribution predictions with no fitting other than a single constant shift. In all panels, max-affine and neural network predictions are shown as blue and red points, respectively. Defect energies predicted by the models are computed using finite-difference approximations with step size  $\delta = 0.5$ . **a** DFT-computed interstitial, vacancy, and substitution energies (all defect classes) versus max-affine and neural network predictions (offset  $C = +1.24$  eV/atom). **b,c** DFT-computed interstitial energies versus predictions (Eq. (8)) for nitrogen (b) and oxygen (c) interstitials. Offsets of  $C = +1.75$  eV/atom in b and  $C = +1.24$  eV/atom in c. **d** DFT-computed oxygen-vacancy energies versus predictions (Eq. (11)) for a range of metal oxides (offset  $C = +1.28$  eV/atom). **e** DFT-computed substitution energies versus predictions (Eq. (5)) for a variety of impurities in Nb (offset  $C = +0.09$  eV/atom).

Vacancy energies quantify the cost of removing an A atom from an  $A_x B_{1-x}$  host. In *ab initio* calculations, this is computed as

$$E_{\text{vac}}^n(A_x B_{1-x} \rightarrow A) = E(A) + E(A_{xn-1} B_{(1-x)n}) - E(A_{xn} B_{(1-x)n}), \quad (10)$$

which approaches in the dilute limit (see Methods),

$$E_{\text{vac}}^{\infty}(A_x B_{1-x} \rightarrow A) = E(A) - E(A_x B_{1-x}) - (1-x) \partial_x^- E(A_x B_{1-x}), \quad (11)$$

where  $\partial_x^-$  is a backward derivative. Substituting the max-affine model yields

$$E_{\text{vac}}^{\text{MA}}(A_x B_{1-x} \rightarrow A) = \tilde{\mu}_A - \tilde{\mu}_B^{A_x B_{1-x}} - (1-2x) \left( \tilde{\mu}_B^{A_x B_{1-x}} - \tilde{\mu}_A^{A_x B_{1-x}} \right). \quad (12)$$

To enable direct comparison with *ab initio* density-functional theory (DFT) calculations, we evaluate the defect-energy expressions derived above, Eqs. (5,8,11), using finite-difference approximations to the compositional derivatives, for both the max-affine and neural network models. We emphasize that in all cases the training data consisted solely of bulk formation energies: no defect energies were included at any stage, so that the results represent true predictions. Finally, for this demonstration, we focus on N and O interstitials in metallic hosts, substitutional defects in Nb metal, and oxygen vacancies in metal oxides, as these systems are chemically relevant, represented in existing DFT datasets, and probe chemically distinct environments.

Across all defect types, both models capture the DFT trends (Fig. 3a), with the neural network achieving slightly lower mean absolute errors, while the max-affine model retains the advantage of interpretability: its predictions depend only on the effective chemical potentials, and thus on the seven facet coefficients that encode the chemical environment of each material. Although the absolute errors remain large compared to typical DFT accuracy, the correlations are sufficiently strong to make these models valuable for rapid, composition-only trend discovery and initial screening in materials searches. The strength of the correlations is notable given the diversity of defect types and the fact that these results represent genuine out-of-distribution predictions.

Systematic downward shifts in the predicted defect energies are observed across all classes, reflecting a convex-hull bias inherited from training on near-hull bulk formation energies. These offsets are largely constant within each defect class and can be corrected by offsets of +1.75 eV/atom for nitrogen interstitials (Fig. 3b), +1.24 eV/atom for oxygen interstitials (Fig. 3c), +1.28 eV/atom for vacancies (Fig. 3d), and +0.09 eV/atom for substitutions (Fig. 3e).

Overall, these results confirm that a composition-only model trained exclusively on bulk formation energies can nonetheless generalize to yield physically meaningful defect energetics. In practice, the ability to operate using composition alone—without structural input—combined with speed and interpretability makes these models particularly powerful for first-pass materials screening. This, in turn, enables rapid down-selection of candidate chemistries prior to any structural modeling or costly first-principles calculations.

### Predicting Elemental Spatial Correlations in High-Entropy Phosphides

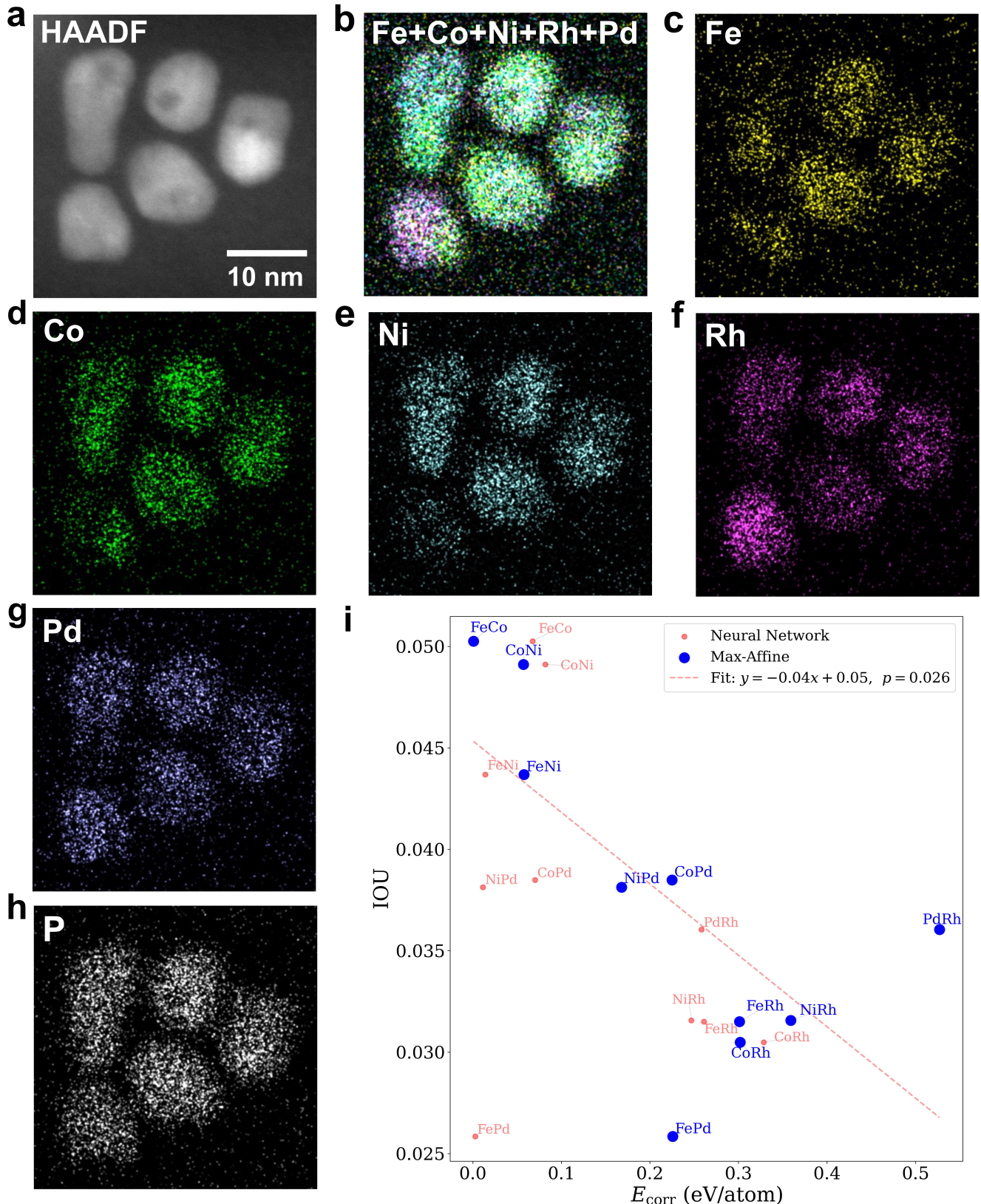
With the above composition-only models in hand, we now turn to a qualitatively different class of phenomena governed by energy differences: elemental spatial correlations in compositionally complex materials. High-entropy materials, by definition, contain five or more elements randomly distributed over a single crystallographic site. In practice, however, local deviations from randomness—such as clustering or chemical ordering—can arise, and have been investigated in compositionally complex alloys through simulations and limited experiments [23–26].

Figure 4 illustrates this effect in our samples. Figure 4a shows a high-angle annular dark-field (HAADF), STEM image of  $(\text{FeCoNiRhPd})_2\text{P}$  high-entropy phosphide nanoparticles, while Figs. 4b–h present the corresponding scanning transmission electron microscopy energy-dispersive X-ray spectroscopy (STEM-EDS) elemental maps for all metal elements in **b** and each constituent element in **c–h**. These maps reveal clear, non-random spatial correlations of varying strength among the metallic species. For example, Fe- and Rh-rich regions exhibit a pronounced anticorrelation, indicating chemically selective local environments within the nanoparticles.

To quantify the experimental correlations in a simple and robust manner, we represent each elemental map as  $I_{\alpha}(p)$ , where  $p$  enumerates the pixels and  $\alpha$  denotes a metallic species. The image intensities are first normalized to lie between 0 and 1, and then thresholded at 0.55 to balance signal retention and noise suppression, with pixels below the cutoff set to zero and those above set to one. We then compute an intersection-over-union (IOU) metric between each pair of elemental masks,

$$\text{IOU}(\alpha, \beta) = \frac{I_{\alpha} \cap I_{\beta}}{I_{\alpha} \cup I_{\beta}}, \quad (13)$$

where  $\cap$  and  $\cup$  denote intersection and union, respectively. This metric is equivalent to the Jaccard similarity coefficient [27], a standard measure of spatial overlap. A high IOU value indicates a correlated pair of elements, while a low value indicates anticorrelation.



**FIG. 4. Elemental spatial correlations in high-entropy phosphide nanoparticles.** **a** High-angle annular dark-field (HAADF) STEM image of high-entropy phosphide nanoparticles. **b–h** Scanning transmission electron microscopy coupled with energy-dispersive X-ray spectroscopy (STEM-EDS) elemental maps of the  $(\text{FeCoNiRhPd})_2\text{P}$  high-entropy phosphide, showing the spatial distribution of all metal elements in **b** and individual elements in **c–h**, respectively, for the same nanoparticles shown in **a**. All elemental maps are acquired from the same particles and are spatially registered to the HAADF image. **i** Intersection-over-union (IOU) values (Eq. (13), threshold 0.55) extracted from the STEM-EDS images, plotted against the correlation energy  $E_{corr}$  descriptor (Eq. (14)) computed using the max-affine (blue) and neural network (red) models. Note that the neural network points are not individually labeled to avoid overcrowding the plot. The red dashed line denotes the line of best fit for the max-affine model, which exhibits a  $p$ -value of 0.026, indicating statistical significance.

Such spatial correlations reflect local energetic competition between elements for a shared chemical environment. This competition is directly encoded in composition-only formation energies, which provide a remarkably flexible quantity from which a broad range of material behaviors can be probed by constructing appropriate energy differences. Specifically, to predict elemental spatial correlations between two elements A and B in a high-entropy phosphide material, we consider the formation energies of the ternary phosphides  $A_{2x/3}B_{2(1-x)/3}P_{1/3}$ . Empirically, we find that both models predict a nearly linear dependence on  $x$ , indicating simple enthalpic mixing and the absence of energetically favored intermediate compositions when mixing entropy is neglected. In this regime, only the slope of the energy with respect to composition is physically relevant, with a large absolute slope reflecting a strong enthalpic preference for phase separation into binary phosphides, making ternary stabilization unlikely and signaling anticorrelation. Conversely, a small slope indicates weak enthalpic driving forces, allowing entropy to stabilize mixed configurations and leading to spatial correlation. These observations motivate the following descriptor, which measures the slope of the energy versus composition curve, as predictive of the degree of correlation between species pairs in the high-entropy phosphide,

$$E_{\text{corr}}(A, B) = |E(A_{2/3}P_{1/3}) - E(B_{2/3}P_{1/3})|. \quad (14)$$

Figure 4i compares the correlation energy  $E_{\text{corr}}$ , computed using the interpretable max-affine model (blue) and the neural network model (red), against the experimental intersection-over-union (IOU) values defined in Eq. (13). As expected, a negative correlation is observed between the IOU and the calculated correlation energy; for the max-affine model, this correlation is statistically significant with a p-value of 0.026. Importantly,  $E_{\text{corr}}$  is a physically motivated descriptor derived solely from composition-only formation energies, and no parameters are fit or adjusted to the experimental correlation data, so the comparison constitutes a genuine out-of-sample test. Figure 4i also highlights several illustrative elemental pairs whose correlation or anticorrelation are readily apparent in the STEM-EDS images: Co–Ni, Fe–Co, and Fe–Ni are spatially correlated, whereas Fe–Rh, Ni–Rh, and Co–Rh are spatially anticorrelated. The observed agreement demonstrates that composition-only models—parameterized here by just seven facet coefficients per element—capture the dominant energetic drivers governing elemental mixing and segregation in high-entropy materials. We anticipate that the same framework can be extended to predict higher-order correlations involving more than two elements, as have been reported in compositionally complex systems [24].

## Pourbaix Diagrams and Optimizing Electrochemical Stability

As a final illustrative application, we apply the max-affine model to the construction of Pourbaix diagrams, which map a material’s electrochemical stability across pH and electrode potential  $V$ . Owing to its combination of flexibility and analytical simplicity, the model not only enables direct prediction of Pourbaix diagrams from formation energies but also allows their targeted optimization.

To compute a Pourbaix diagram, one enumerates all plausible aqueous decomposition reactions of the given material into oxide, hydroxide, or hydride products plus protons and electrons. The modified free energy of any such reaction at pH and potential  $V$  is found using the Nernst equation

$$G_{\text{mod}} = \sum_{i \in P} E_i - \sum_{i \in R} E_i + 0.059 \left( \log_{10} \left( \frac{[P]}{[R]} \right) - N_{\text{H}^+} \text{pH} \right) - N_{e^-} V \quad (15)$$

where  $E_i$  is the formation energy of species  $i$  (obtained from the max-affine model, from experiment, or from DFT),  $P$  denotes the products,  $R$  denotes the reactants,  $[ \cdot ]$  denotes activity (ions:  $10^{-6}$ ; solids: 1),  $N_{\text{H}^+}$  is the number of hydrogen atoms, and  $N_{e^-}$  is the number of electrons. At each  $(\text{pH}, V)$  combination, the reaction with the lowest  $G_{\text{mod}}$  defines the thermodynamically stable phase.

Fig. 5a shows the Pourbaix diagram for Ti constructed using formation energies for solid phases predicted by the max-affine model, together with tabulated experimental formation energies for solvated ions, while Fig. 5b shows the corresponding diagram constructed entirely from experimental formation energies [28, 31]. We observe strong agreement between the predicted and experimental stability regions, lending confidence to the ability of the max-affine model to reproduce electrochemical phase stability.

We next extend this approach to binary alloys of the form  $A_\alpha B_{1-\alpha}$ , for which oxidation under electrochemical conditions need not proceed through a single, stoichiometrically fixed oxide phase. Unlike elemental metals, binary alloys can lower their free energy through partial oxidation and the formation of mixed-metal oxides with variable oxygen content. To capture this behavior efficiently, we represent oxidation using a continuous parameter  $\eta \in [0, 1]$  denoting the fraction of oxygen incorporated into the solid. The corresponding oxidized composition is written as  $A_{\alpha(1-\eta)}B_{(1-\alpha)(1-\eta)}O_\eta$ , which preserves the relative metal stoichiometry while allowing the oxygen content to vary continuously.

To reference energies consistently per formula unit of

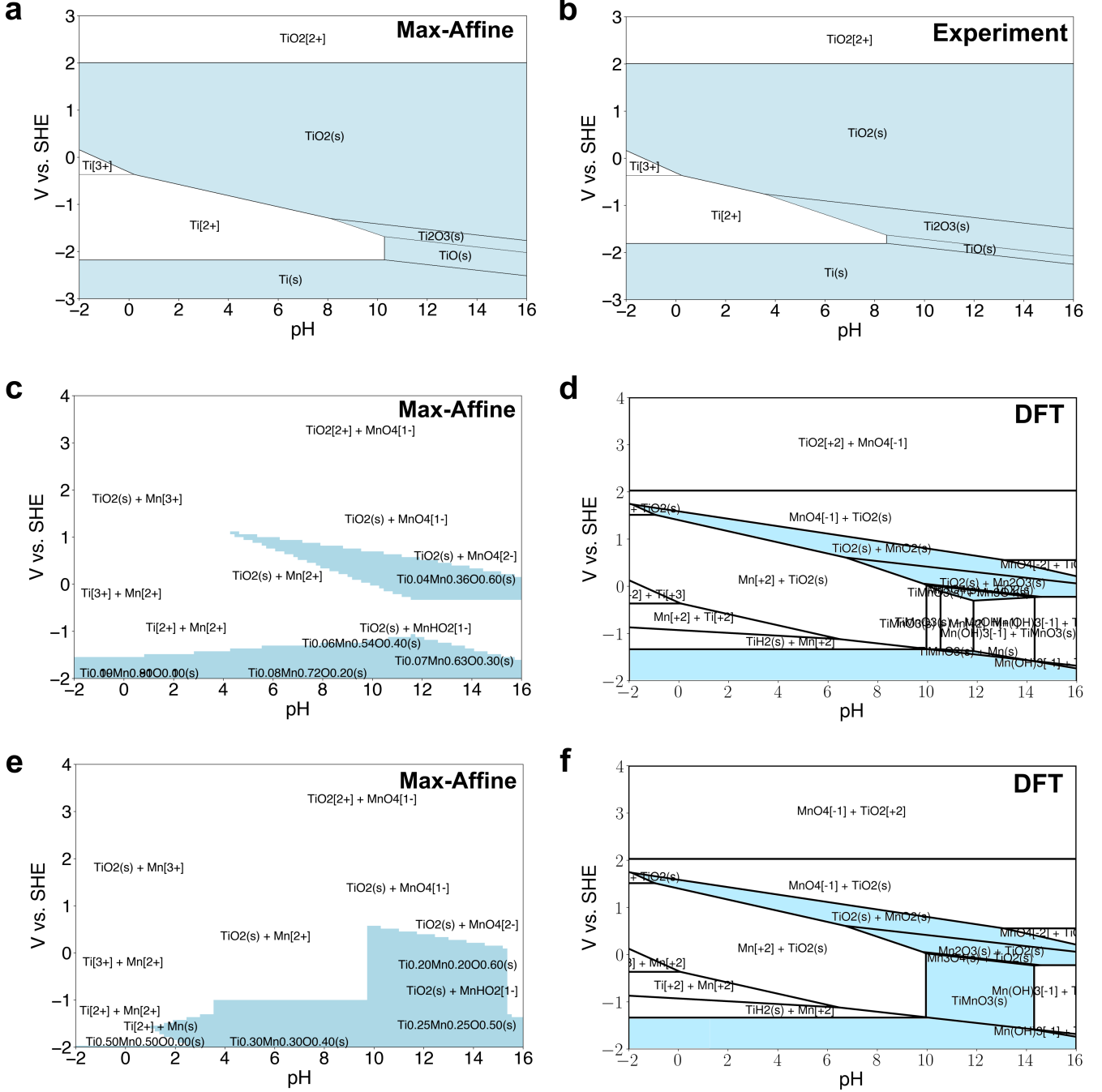


**FIG. 5. Predicted versus experimental and DFT-calculated Pourbaix diagrams.** **a** Pourbaix diagram for Ti constructed using max-affine model predictions for solid phases. **b** Pourbaix diagram for Ti constructed using experimental formation energies for solid phases. **c** Pourbaix diagram for  $\text{Ti}_{0.1}\text{Mn}_{0.9}$  constructed using max-affine model predictions for solid phases. **d** Pourbaix diagram for  $\text{Ti}_{0.1}\text{Mn}_{0.9}$  constructed using the Materials Project Pourbaix diagram tool [28–30], which employs DFT-calculated formation energies. **e** Pourbaix diagram for  $\text{Ti}_{0.5}\text{Mn}_{0.5}$  constructed using max-affine model predictions for solid phases. This composition is identified by rapid, composition-only optimization as having the largest stable region within the electrochemical window of water at high pH. **f** Pourbaix diagram for  $\text{Ti}_{0.5}\text{Mn}_{0.5}$  constructed using the Materials Project Pourbaix diagram tool. In all panels, blue shaded regions indicate thermodynamically stable solid phases, while white regions correspond to stable aqueous ionic species.

the parent alloy, we normalize by  $1/(1 - \eta)$ . The modified free energy of oxidation at a given pH and electrode potential  $V$  is then

$$G_{\text{mod}}(\eta) = \frac{1}{1 - \eta} E(A_{\alpha(1-\eta)} B_{(1-\alpha)(1-\eta)} O_{\eta}) - E(A_{\alpha} B_{1-\alpha}) - \frac{\eta}{1 - \eta} E(H_2O) - 2 \frac{\eta}{1 - \eta} (0.059 \text{ pH} - V), \quad (16)$$

where  $E(H_2O) = -2.46 \text{ eV/fu}$  [28]. For fixed alloy composition  $\alpha$ , pH, and potential  $V$ , we minimize  $G_{\text{mod}}(\eta)$  to determine the most stable degree of oxidation,  $\eta^*$ . This minimum free energy is then compared against all competing aqueous decomposition reactions at each  $(\text{pH}, V)$  grid point to assign the thermodynamically stable phase. (Further details are provided in Methods.)

As a concrete demonstration of this framework, we apply the above construction to the binary alloy system  $Ti_{\alpha}Mn_{1-\alpha}$ . For simplicity in this initial demonstration, the max-affine-based optimization considers only the stability of the ternary oxide and neglects competitive decomposition into separate  $Ti\text{-O}$  and  $Mn\text{-O}$  binary oxides. Because the max-affine model operates directly on composition, requires no structural optimization, and is linear with a limited number of parameters, it enables rapid exploration of alloy composition space and renders targeted optimization for electrochemical stability computationally tractable. Leveraging this efficiency, we scan alloy compositions  $\alpha = 0.1, 0.2, \dots, 0.9$  and identify  $Ti_{0.5}Mn_{0.5}$  as exhibiting the largest region of electrochemical stability within the electrochemical window of water at high pH. Figures 5c and d compare the max-affine-predicted (neglecting competitive binary-oxide decomposition) and DFT-calculated Pourbaix diagrams for  $Ti_{0.1}Mn_{0.9}$ , while Figs. 5e and f show the corresponding comparison for the compositionally optimized alloy  $Ti_{0.5}Mn_{0.5}$ . In both cases, apart from competitive binary-oxide decomposition intentionally neglected during the optimization, the predicted diagrams closely reproduce the DFT-based stability regions of the solid phases, demonstrating that the composition-only max-affine model can guide the optimization of alloy compositions under electrochemical conditions.

## DISCUSSION

In this work, we have shown that the thermodynamic stability of inorganic materials across composition space exhibits a striking and previously unrecognized simplicity. The convex hull of formation energies can be accurately approximated by a max-affine model with only seven linear facets, corresponding to seven coefficients per element. This representation reproduces near-hull formation energies at close to density functional theory

(DFT) accuracy while remaining fully interpretable. Importantly, the rapid saturation of predictive accuracy with facet number suggests that these seven facets are not merely sufficient to fit the data, but instead reflect a small set of underlying, dominant chemical families that govern thermodynamic stability across multi-element materials classes. Finally, the coefficients defining each facet have a natural interpretation as distinct sets of effective compositional chemical potentials, ensuring consistent chemical behavior aligned with periodic-table trends for the materials on each facet.

Beyond reproducing bulk thermodynamic stability, the composition-only model demonstrates a surprising degree of transferability across a range of materials phenomena. Without retraining or structural input, the same parameterization captures systematic trends in defect formation energies, reproduces experimentally observed elemental correlations in high-entropy materials, and enables the construction and optimization of electrochemical stability diagrams. Together, these demonstrations highlight the practical utility of the model as a transferable, interpretable framework for navigating complex composition spaces.

Despite this breadth of transferability, the present formulation is not without limitations. Training predominantly on near-hull data introduces systematic stabilization biases, necessitating constant offsets when comparing absolute defect energies to DFT. Sparse sampling in certain regions of composition space can blur facet assignments, and explicit finite-temperature entropies are not included. These limitations, however, suggest clear and tractable extensions, such as calibrating offsets using small reference datasets or attaching uncertainty estimates to identify out-of-distribution compositions and guide targeted data acquisition.

Taken together, our results demonstrate that a remarkably small set of interpretable parameters can approximate a broad range of DFT-derived and experimentally relevant thermodynamic observables. By exposing the low-complexity geometric structure underlying the formation-energy landscape, the max-affine framework reframes composition-only modeling as a general, geometry-free thermodynamic description, offering both predictive power and physical insight across diverse materials phenomena. Viewed through this lens, the formation-energy landscape of inorganic materials is not arbitrarily complex, but instead organized into a small number of chemically meaningful regimes—revealing that much of solid-state thermodynamics near stability can be understood and optimized using composition alone.

## METHODS

### Dataset Preparation

To construct the training set for the neural network model, we start from bulk inorganic compounds in the Materials Project database [2] with density functional theory (DFT)-computed formation energies. For each composition, only the lowest-energy structure is retained. We then restrict the dataset to materials containing between one and five elements and discard any compound lying more than 0.25 eV/atom above the convex hull, yielding a final dataset of 86,925 compounds. This dataset is randomly split into 80% training and 20% test sets. The dataset used to train the max-affine model is constructed using the same Materials Project dataset, but with a more stringent stability criterion. Specifically, we retain only compounds within 0.025 eV/atom of the convex hull, reflecting the model’s focus on near-hull thermodynamic behavior. This filtering results in a dataset of 51,068 compounds, which is likewise split into 80% training and 20% test sets.

### Model Training

We train the neural network using PyTorch [32] with the Adam optimizer [33] (learning rate  $1 \times 10^{-3}$ ), mean squared error loss, and a batch size of 512. Training is run for 1,000 epochs to convergence, with a weight decay of  $1 \times 10^{-8}$  to promote smoothness and improve generalization.

The max-affine model is trained using the same optimization framework in PyTorch, again employing the Adam optimizer (learning rate  $1 \times 10^{-3}$ ), mean squared error loss, and a batch size of 512. Training is run for 1,600 epochs to convergence. In practice, we train a softened version of Eq. (2),

$$E(\mathbf{x}) = \tau \log \left( \sum_{f=1}^F \exp \left[ \frac{\sum_{s=1}^{92} a_{fs} x_s}{\tau} \right] \right) + b, \quad (17)$$

where  $\tau > 0$  is a temperature parameter. During training,  $\tau$  is gradually decreased to approach the hard max-affine model of Eq. (2). The  $\tau \rightarrow 0$  limit, when Eq. (17) becomes Eq. (2), is taken after training.

### Ab initio Calculations

All density functional theory (DFT) calculations of point defects were carried out using the JDFTx [34] code. For interstitial and vacancy formation energies,  $2 \times 2 \times 2$  or  $3 \times 3 \times 3$  supercells (depending on the parent lattice symmetry) were generated from conventional unit cells

obtained via the Materials Project API. Substitution energies were evaluated in Nb supercells with a single metal replacement, and oxygen vacancies were modeled by removing one O atom from a  $2 \times 2 \times 2$  metal oxide supercell. Ionic cores were described using the GBRV ultrasoft PBE potentials for interstitial and vacancy calculations and the SG15 ONCV PBE library for substitution energies [35, 36]. Plane-wave cutoffs of 20 H for wavefunctions (100 H for charge density) were used for interstitial and vacancy calculations, while cutoffs of 30 H (200 H for charge density) were used for substitution energies, ensuring total-energy convergence to within  $10^{-5}$  H. A  $\mathbf{k}$ -point grid of  $4 \times 4 \times 4$  was employed, together with a Fermi–Dirac smearing corresponding to an effective temperature of  $4 \times 10^{-3}$  H. Complete information about all calculations—including final atomic coordinates, total energies, and input parameters—is available on the GitHub repository.

### Defect Energies from Composition-Only Formation Energies

We first derive the substitution energy expression in Eq. (5). Starting from the finite- $n$  definition in Eq. (4) and using the extensivity of the energy,  $E(xM) = xE(M)$ , we rewrite the substitution energy as

$$\begin{aligned} E_{\text{sub}}^n(A \leftarrow B) &= E(A_{n-1}B) + E(A) - (E(A_n) + E(B)) \\ &= E(A) - E(B) \\ &\quad + n \left[ E(A_{1-\frac{1}{n}}B_{\frac{1}{n}}) - E(A) \right]. \end{aligned} \quad (18)$$

Introducing  $\delta = 1/n$ , we expand the energy about  $\delta = 0$  and take the  $n \rightarrow \infty$  (i.e.,  $\delta \rightarrow 0^+$ ) limit,

$$\begin{aligned} E_{\text{sub}}^\infty(A \leftarrow B) &= E(A) - E(B) \\ &\quad + \frac{1}{\delta} \left[ E(A_{1-\delta}B_\delta) - E(A) \right] \\ &\quad + \mathcal{O}(\delta). \end{aligned}$$

Taking the limit  $\delta \rightarrow 0$  yields

$$E_{\text{sub}}^\infty(A \leftarrow B) = E(A) - E(B) + \partial_\delta^+ E(A_{1-\delta}B_\delta) \Big|_{\delta=0},$$

recovering Eq. (5). We note that a *forward* derivative  $\partial^+$  must be used, since the perturbation  $\delta = 1/n > 0$ .

We next derive the dilute-limit interstitial energy expression in Eq. (8). Starting from a bulk host containing  $n-1$  atoms and again using extensivity, the finite-size interstitial energy Eq. (7) is

$$\begin{aligned} E_{\text{int}}^{n-1}(A \leftarrow B) &= E(A_{n-1}B) - (E(A_{n-1}) + E(B)) \\ &= E(A_{n-1}B) + E(A) - (E(A_n) + E(B)), \end{aligned}$$

which is identical in form to the starting point of Eq. (18). This explains why the substitutional and interstitial energies in the main text, Eqs. (5) and (8), have exactly

the same form in the dilute limit  $n \rightarrow \infty$ . Physically, the reason is that the ground-state formation energy function  $E(\mathbf{x})$  implicitly encodes the lowest-energy mechanism by which an impurity is incorporated into the host lattice, whether substitutional or interstitial.

Finally, we derive the vacancy–energy expression in Eq. (11). Starting from the finite- $n$  form in Eq. (10), we rewrite it using extensivity as

$$\begin{aligned} E_{\text{vac}}^n(A_x B_{1-x} \rightarrow A) &= E(A) + E(A_{xn-1} B_{(1-x)n}) - E(A_{xn} B_{(1-x)n}), \\ &= (n-1)E\left(A_{x-\frac{1-x}{n-1}} B_{1-x+\frac{1-x}{n-1}}\right) \\ &\quad + E(A) - nE(A_x B_{1-x}). \end{aligned}$$

Note that  $(1-x)/(n-1) \geq 0$ , so the physically admissible perturbation always *decreases* the fraction of A and *increases* the fraction of B.

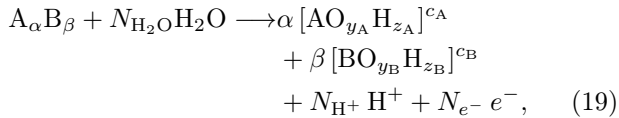
Defining  $\delta = 1/(n-1) > 0$  and expanding about  $\delta = 0$  yields

$$\begin{aligned} E_{\text{vac}}^\infty(A_x B_{1-x} \rightarrow A) &= E(A) - E(A_x B_{1-x}) \\ &\quad - (1-x) \partial_x^- E(A_x B_{1-x}) + \mathcal{O}(\delta), \end{aligned}$$

where  $\partial_x^-$  denotes the *backward* derivative with respect to  $x$ . Here, the backward derivative is required because the admissible perturbation moves leftward along the composition axis—a forward or central difference would probe compositions to the right of  $x$ , which are inaccessible under this construction and would therefore misrepresent the relevant local slope of the formation–energy curve. Finally, discarding  $\mathcal{O}(\delta)$  terms recovers Eq. (11).

### Pourbaix Diagram Construction

We generate Pourbaix diagrams for unary or binary materials (e.g. Ti, Ti<sub>0.1</sub>Mn<sub>0.9</sub>) by (1) enumerating all candidate aqueous products, (2) computing their formation energies using the max-affine or neural network model (Eq. (2)), and (3) selecting the phase with the minimum modified free energy  $G_{\text{mod}}$  over a grid of pH and electrode potential  $V$ . We consider the following general form of ion-forming reactions involving a binary material A <sub>$\alpha$</sub> B <sub>$\beta$</sub>  ( $\beta \equiv 1 - \alpha$ ),

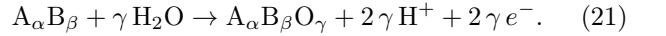


where  $N_{\text{H}_2\text{O}}$ ,  $N_{\text{H}^+}$ , and  $N_{e^-}$  denote the numbers of water molecules, hydrogen ions, and electrons involved in the reaction, respectively. The quantities  $c_A$  and  $c_B$  denote the charges of the aqueous products containing A and B, while  $y_A$ ,  $z_A$ ,  $y_B$ , and  $z_B$  are the stoichiometric

coefficients of oxygen and hydrogen in the corresponding products. Mass and charge balance impose

$$\begin{aligned} N_{\text{H}_2\text{O}} &= \alpha y_A + \beta y_B \\ N_{\text{H}^+} &= 2N_{\text{H}_2\text{O}} - \alpha z_A - \beta z_B \\ N_{e^-} &= N_{\text{H}^+} + \alpha c_A + \beta c_B \end{aligned} \quad (20)$$

For reactions forming a solid ternary oxide A <sub>$\alpha$</sub> B <sub>$\beta$</sub> O <sub>$\gamma$</sub> , we instead write



To align the max-affine model energies with experimental ion free energies, we apply constant offsets determined by comparing DFT formation energies from the Materials Project—on which the model was trained—to experimental formation energies of reference oxides, following the procedure of Ref. [28]. Because the Materials Project does not include ionic formation energies, we use experimental values for all aqueous species when constructing Pourbaix diagrams. The offsets we apply to experimental ionic formation energies are obtained by taking the differences between experimental data [31] and DFT energies [2], with experimental values taken from Refs. [28, 31].

### Synthesis of high-entropy phosphide nanoparticles

First, precursor solutions were prepared by dissolving each metal salt [36.5 mg Co(acac)<sub>3</sub>, 27.0 mg Ni(acac)<sub>2</sub>, 42.2 mg Rh(acac)<sub>3</sub>, 32.2 mg PdCl<sub>2</sub>, 36.5 mg Fe(acac)<sub>3</sub>] in 10 mL of oleylamine with gentle heating and sonication. Next, a 50-mL three-neck round-bottom flask was assembled with a thermocouple, reflux condenser, gas flow adapter, and rubber septum; 10 mL of 1-octadecene (ODE) and 6 mL of oleylamine (OLAM) were added and degassed under vacuum at 110 °C for 1 hour. The system was then purged by alternating argon and vacuum three times, followed by heating under a continuous argon flow to 320 °C. After this step, 1 mL of the Ni(acac)<sub>2</sub> solution and 0.75 mL of each of the remaining metal precursor solutions were combined, degassed under vacuum for 15 minutes, purged three times with argon and vacuum, and rapidly injected into the 50 mL reaction flask containing ODE and OLAM at 320 °C. The reaction was held at 315 °C for 1.5 hours, cooled to 220 °C, and quenched in a room-temperature water bath. The product was isolated by washing twice with a 1:2 (v/v) mixture of toluene and ethanol, followed by centrifugation and redispersion in toluene after each wash. The purified nanoparticles were suspended and stored in toluene. High-angle annular dark-field scanning transmission electron microscopy (HAADF-STEM) images and corresponding STEM energy-dispersive X-ray spectroscopy (STEM–EDS) elemental maps were acquired using an FEI Talos F200X S/TEM operated at

an accelerating voltage of 200 kV. The STEM-EDS data were processed and analyzed using Velox 3.6.0 software. Elemental mapping and analysis were performed using the Fe K $\alpha$ , Co K $\alpha$ , Ni K $\alpha$ , Rh L $\alpha$ , and Pd L $\alpha$  characteristic energy lines.

## DATA AVAILABILITY

The datasets generated and/or analysed during the current study are available in the Max-Affine-Data repository, <https://github.com/jt577/Max-Affine-Data>.

## CODE AVAILABILITY

The underlying code for this study is available in Max-Affine-Data and can be accessed via this link <https://github.com/jt577/Max-Affine-Data>.

---

[1] S. Curtarolo, G. L. W. Hart, M. B. Nardelli, N. Mingo, S. Sanvito, and O. Levy, *Nature Materials* **12**, 191 (2013).

[2] A. Jain, S. P. Ong, G. Hautier, W. Chen, W. D. Richards, S. Dacek, S. Cholia, D. Gunter, D. Skinner, G. Ceder, and K. A. Persson, *APL Materials* **1**, 011002 (2013).

[3] J. E. Saal, S. Kirklin, M. Aykol, B. Meredig, and C. Wolverton, *Jom* **65**, 1501 (2013).

[4] A. R. Oganov and C. W. Glass, *Journal of Chemical Physics* **124**, 244704 (2006).

[5] S. M. Woodley and R. Catlow, *Nature materials* **7**, 937 (2008).

[6] M. C. Payne, M. P. Teter, D. C. Allan, T. A. Arias, and J. D. Joannopoulos, *Rev. Mod. Phys.* **64**, 1045 (1992).

[7] L. Chanussot, A. Das, S. Goyal, T. Lavril, M. Shuaibi, M. Riviere, K. Tran, J. Heras-Domingo, C. Ho, W. Hu, A. Palizhati, A. Sriram, B. Wood, J. Yoon, D. Parikh, C. L. Zitnick, and Z. Ulissi, *ACS Catalysis* **11**, 6059 (2021).

[8] R. Tran, J. Lan, M. Shuaibi, B. M. Wood, S. Goyal, A. Das, J. Heras-Domingo, A. Kolluru, A. Rizvi, N. Shoghi, A. Sriram, F. Therrien, J. Abed, O. Voznyy, E. H. Sargent, Z. Ulissi, and C. L. Zitnick, *ACS Catalysis* **13**, 3066 (2023).

[9] S. Curtarolo, W. Setyawan, S. Wang, J. Xue, K. Yang, R. H. Taylor, L. J. Nelson, G. L. W. Hart, S. Sanvito, M. Buongiorno-Nardelli, N. Mingo, and O. Levy, *Computational Materials Science* **58**, 227 (2012).

[10] K. Choudhary, K. F. Garrity, A. C. E. Reid, B. DeCost, A. J. Biacchi, A. R. Hight Walker, Z. Trautt, J. Hattrick-Simpers, A. G. Kusne, A. Centrone, A. Davydov, J. Jiang, R. Pachter, G. Cheon, E. Reed, A. Agrawal, X. Qian, V. Sharma, H. Zhuang, S. V. Kalinin, B. G. Sumpter, G. Pilania, P. Acar, S. Mandal, D. Vanderbilt, K. Rabe, and F. Tavazza, *npj Computational Materials* **6**, 173 (2020).

[11] T. Xie and J. C. Grossman, *Physical Review Letters* **120**, 145301 (2018).

[12] K. T. Schütt, H. E. Sauceda, P.-J. Kindermans, A. Tkatchenko, and K.-R. Müller, *Journal of Chemical Physics* **148**, 241722 (2018).

[13] C. Chen, W. Ye, Y. Zuo, C. Zheng, and S. P. Ong, *Chemistry of Materials* **31**, 3564 (2019).

[14] J. Gasteiger, J. Gross, and S. Gunnemann, in *International Conference on Learning Representations (ICLR)* (2020).

[15] G. Cheng, X.-G. Gong, and W.-J. Yin, *Nature Communications* **13**, 1492 (2022).

[16] K. Choudhary and B. DeCost, *npj Computational Materials* **7**, 10.1038/s41524-021-00650-1 (2021).

[17] C. Zeni, R. Pinsler, D. Zügner, A. Fowler, M. Horton, X. Fu, Z. Wang, A. Shysheya, J. Crabbé, S. Ueda, R. Sordillo, L. Sun, J. Smith, B. Nguyen, H. Schulz, S. Lewis, C.-W. Huang, Z. Lu, Y. Zhou, H. Yang, H. Hao, J. Li, C. Yang, W. Li, R. Tomioka, and T. Xie, *Nature* **639**, 624 (2025).

[18] D. Jha, L. Ward, A. Paul, W. K. Liao, A. Choudhary, C. Wolverton, and A. Agrawal, *Scientific Reports* **8**, 17593 (2018).

[19] R. E. A. Goodall and A. A. Lee, *Nature Communications* **11**, 10.1038/s41467-020-19964-7 (2020).

[20] S. Sun and Others, *Iynet: Individual residual learning for deep networks in materials property prediction*, Under review, *Science Advances* (2020).

[21] A. Y.-T. Wang, S. K. Kauwe, R. J. Murdock, and T. D. Sparks, *npj Computational Materials* **7**, 77 (2021).

[22] S. Chaudhari, C. Méndez, R. Choudhary, T. Banerjee, M. W. Olszewski, J. T. Paustian, J. Choi, Z. Baraissov, R. Hernandez, D. A. Muller, B. L. T. Plourde, G. D. Fuchs, V. Fatemi, and T. A. Arias, *Active-learning inspired Ab Initio theory-experiment loop approach for management of material defects: Application to superconducting qubits* (2025), arXiv:2510.02544 [cond-mat.mtrl-sci].

[23] A. Ferrari, F. Körmann, M. Asta, and J. Neugebauer, *Nature Computational Science* **3**, 221 (2023).

[24] Q. Ding, Y. Zhang, X. Chen, X. Fu, D. Chen, S. Chen, L. Gu, F. Wei, H. Bei, Y. Gao, M. Wen, J. Li, Z. Zhang, T. Zhu, R. O. Ritchie, and Q. Yu, *Nature* **574**, 223 (2019).

[25] Y. Ma, Q. Wang, C. Li, L. J. Santodonato, M. Feygenson, C. Dong, and P. K. Liaw, *Scripta Materialia* **144**, 64 (2018).

[26] S. L. A. Bueno, A. Leonardi, N. Kar, K. Chatterjee, X. Zhan, C. Chen, Z. Wang, M. Engel, V. Fung, and S. E. Skrabalak, *ACS Nano* **16**, 18873 (2022), pMID: 36255141, <https://doi.org/10.1021/acsnano.2c07787>.

[27] P. Jaccard, *Bulletin de la Société Vaudoise des Sciences Naturelles* **37**, 547 (1901).

[28] K. A. Persson, B. Waldwick, P. Lazic, and G. Ceder, *Phys. Rev. B* **85**, 235438 (2012).

[29] A. M. Patel, J. K. Nørskov, K. A. Persson, and J. H. Montoya, *Phys. Chem. Chem. Phys.* **21**, 25323 (2019).

[30] A. K. Singh, L. Zhou, A. Shinde, S. K. Suram, J. H. Montoya, D. Winston, J. M. Gregoire, and K. A. Persson, *Chemistry of Materials* **29**, 10159 (2017).

[31] M. Pourbaix, *Atlas of Electrochemical Equilibria in Aqueous Solutions*, 2nd ed. (National Association of Corrosion Engineers, Houston, TX, 1974).

[32] A. Paszke, S. Gross, F. Massa, A. Lerer, J. Bradbury, G. Chanan, T. Killeen, Z. Lin, D. Tompson, E. Lowe, et al., in *Advances in Neural Information Processing Sys-*

tems (2019) pp. 8024–8035.

[33] D. P. Kingma and J. Ba, CoRR **abs/1412.6980** (2014).

[34] R. Sundararaman, K. Letchworth-Weaver, K. A. Schwarz, D. Gunceler, Y. Ozhabes, and T. A. Arias, SoftwareX **6**, 278 (2017).

[35] J. P. Perdew, K. Burke, and M. Ernzerhof, Phys. Rev. Lett. **77**, 3865 (1996).

[36] M. Schlipf and F. Gygi, Computer Physics Communications **196**, 36 (2015).

## ACKNOWLEDGEMENTS

J.T., S.K., R.S., H.A., and T.A. disclose support for the research of this work from the Center for Alkaline-Based Energy Solutions (CABES), part of the Energy Frontier Research Center (EFRC) program supported by the U.S. Department of Energy under grant DE-SC-0019445. S.C. and C.M. disclose support for the research of this work from the US National Science Foundation (NSF) under award PHY-1549132, the Center for Bright

Beams (CBB).

## AUTHOR CONTRIBUTIONS

J.T. conceived and trained all models, and edited the manuscript. S.C. derived the vacancy energy expression and helped J.T. in predicting vacancy energies. C.M. and R.C. performed defect DFT calculations. S.K. and R.S. synthesized and imaged the high entropy phosphide nanoparticles, and edited the corresponding sections of the manuscript. H.A. and P.F. supervised the study. T.A. conceived and supervised the study, and edited the manuscript. All authors reviewed the manuscript.

## COMPETING INTERESTS

All authors declare no financial or non-financial competing interests.